Vortex Beam Generation by Spin-Orbit Interaction with Bloch Surface Waves

Vortex beam generation by spin-orbit coupling in Bloch surface waves

Ugo Stella[1], Thierry Grosjean[2], Natascia De Leo[3], Luca Boarino[3], Peter Munzert[4], Joseph R. Lakowicz[5] and Emiliano Descrovi[1]*

[1] Department of Applied Science and Technology (DISAT), Politecnico di Torino, Corso Duca degli Abruzzi 24, Torino, IT-10129, Italy.

[2] FEMTO-ST Institute, Université Bourgogne Franche-Comté, UMR CNRS 6174 15B Avenue des Montboucons, 25030, Besançon, France

[3] Quantum Research Labs & Nanofacility Piemonte, Nanoscience & Materials Division, Istituto Nazionale di Ricerca Metrologica (INRiM), Strada delle Cacce 91, Torino, IT-10135, Italy.

[4] Fraunhofer Institute for Applied Optics and Precision Engineering IOF, Albert-Einstein-Str. 7, Jena DE-07745, Germany

[5] Center for Fluorescence Spectroscopy, Department of Biochemistry and Molecular Biology, University of Maryland School of Medicine, Baltimore, Maryland 21201, United States

Mr. Ugo Stella: ugo.stella@polito.it

Dr. Thierry Grosjean: thierry.grosjean@univ-fcomte.fr

Dr. Natascia De Leo: n.deleo@inrim.it

Dr. Luca Boarino: l.boarino@inrim.it

Dr. Peter Munzert: peter.munzert@iof.fraunhofer.de

Prof. Joseph R. Lakowicz: JLakowicz@som.umaryland.edu

Corresponding Author:

Prof. Emiliano Descrovi: emiliano.descrovi@polito.it

Phone: +39 011 090 7352

Fax: +39 011 090 7399

Keywords: Chiral nanostructures, Bloch Surface Waves, vortex beam

ABSTRACT

Axis-symmetric grooves milled in metallic slabs have been demonstrated to promote the transfer of Orbital Angular Momentum (OAM) from far- to near-field and vice versa, thanks to spin-orbit coupling effects involving Surface Plasmons (SP). However, the high absorption losses and the polarization constraints, which are intrinsic in plasmonic structures, limit their effectiveness for applications in the visible spectrum, particularly if emitters located in close proximity to the metallic surface are concerned. Here, an alternative mechanism for vortex beam generation is presented, wherein a free-space radiation possessing OAM is obtained by diffraction of Bloch Surface Waves (BSWs) on a dielectric multilayer. A circularly-polarized laser beam is tightly focused on the multilayer backside by means of an immersion optics, such that TE-polarized BSWs are launched radially from the focused spot. While propagating on the multilayer surface, BSWs exhibit a spiral-like wavefront due to the polarization-selective coupling mechanism. A spiral grating surrounding the illumination area provides for the BSW diffraction out-of-plane, by imparting an additional azimuthal geometric phase distribution defined by the topological charge of the spiral structure. At infinity, the constructive interference results into free-space beams with defined combinations of polarization and OAM satisfying the conservation of the Total Angular Momentum, based on the incident polarization handedness and the spiral grating topological charge. As an extension of this concept, chiral diffractive structures for BSWs can be used in combination with surface cavities hosting light sources therein.

INTRODUCTION

Vortex beams represent a family of structured beams generally characterized by a phase singularity along the optical axis, a doughnut intensity distribution and an azimuthally-varying phase over a beam transverse cross-section [1,2]. When the polarization state is spatially inhomogeneous, the term Vectorial Vortex Beams is often used [3]. From a quantum-optics perspective, each vortex beam photon is provided with a quantized Orbital Angular Momentum (OAM) equal to $\hbar\ell$, where ℓ is an integer indicating the topological charge of the vortex. In recent years, Vortex beams have gained an increasing popularity because of several new applications into different domains such as micro-particle manipulation and trapping [4-6], compact laser sources [7,8], microscopy [9,10] and optical communications [11,12]. Conventional methods for producing vortex beams [13] involve the use of (possibly tunable) anisotropic media such as Liquid Crystal [14,15] and q-plates [16] or hierarchically structured holograms encoding proper phase functions [17-20]. More recently, metasurfaces, which can be either dielectric or plasmonic, have been introduced in order to gather more degrees of freedom in OAM manipulation [21,22], through the control of so-called spin-orbit coupling effects mediated by the metasurface topology [23]. Metasurfaces are mainly employed as free-space beam converters, which have found applications also within laser cavities [24]. The concept of beam conversion through metasurfaces relies on a spatially-dependent phase manipulation of the scattered field. The output vortex beams result from a coherent sum of the scattered radiation originating from different portions of the surface, which is illuminated as a whole. However, this approach can be hardly adopted when the input field has a limited spatial extension (as for focused beams or localized coherent sources such as optical antennas or cavities), unless some mode coupling is intervening [25]. This is indeed the case in structured metallic films, wherein the generation of free-space vortex beam carrying OAM occurs upon spin-orbit coupling and scattering/diffraction of plasmonic modes by means of nano-slits [26-28], properly arranged nano-apertures [29], possibly combined with circular diffraction gratings [30,31]. Such results rely on the fact that OAM possessed by surface plasmons can be further manipulated and transferred to freely propagating radiation [28,32].

Here we propose an alternative way of producing vortex beam, by exploiting Bloch Surface Waves [33,34] on dielectric multilayers as a mean to transfer energy, momentum and OAM to a free-space propagating beam. Such a two-step process involves a spin-orbit conversion from a focused circularly polarized beam into radially propagating BSWs and a BSW diffraction in free-space, with an additional geometric phase imparted by a chiral diffraction grating. Such a BSW-based approach can benefit from the multilayer low absorption that is potentially suitable for light source integration and an additional degree of freedom in the polarization state of coupled BSWs, which can be either TE- or TM-polarized depending on the multilayer design [35].

The setup and the sample structure are shown in Figure 1 and described in detail in the Methods section. Briefly, in Figure 1a, a circularly polarized Gaussian CW laser beam (λ=532 nm) is expanded and spatially filtered by means of a properly sized circular Beam Blocker. An oil-immersion, high NA objective is back-contacted to a multilayer glass substrate, in order to focus the incoming beam onto a flat area of the top surface. The multilayer is made of a stack of multiple Ta_2O_5 and SiO_2 layers, topped by a 75 nm-thick PMMA film (Figure 1b,c). Thanks to the beam blocker, only focused light propagating at angles larger than the glass/air critical angle θ_c can reach the sample. A fraction of the incoming power is thus available for coupling to BSWs, provided that wavelength, momentum and polarization matching conditions are fulfilled, as indicated by the BSW dispersion curve for TE-polarization [36]. Since the coupling mechanism is polarization-sensitive and the incident electric field is circularly polarized, BSWs are spreading radially from the focused spot area, with an accumulated phase delay that is linearly varying with the azimuthal angle of the propagation direction. As a result, a BSW propagating radially on the multilayer surface is obtained, with a peculiar spiral-like wavefront profile (see Supporting Information), analogous to plasmonic vortices [26]. Surrounding the flat coupling region, an axis-symmetric diffractive grating is etched in the PMMA layer. The grating operates as an outcoupler, by diffracting BSWs out-of-plane in both substrate (glass) and cladding (air) media, along a direction close-to-normal to the sample surface (order of diffraction n=-1) [37]. Depending on the grating shape (e.g. circular or spiral-like), an additional geometrical phase profile can be imparted to the diffracted radiation. In previous applications, this feature has been exploited for steering the diffracted beam [38,39]. The outcoupled power is then collected by the same high-NA objective and Fourier-transformed before being imaged on the camera plane. A linear polarizer and a quarter-wave plate allow for a polarization analysis on the collected images. If the beam blocker is removed, an interference pattern as shown in Figure 1 can be obtained. In this exemplary case, the spiral-shaped interference fringes result from the superposition of a diffracted vortex beam (OAM number $\ell = 1$) and light reflected from the sample surface [32].

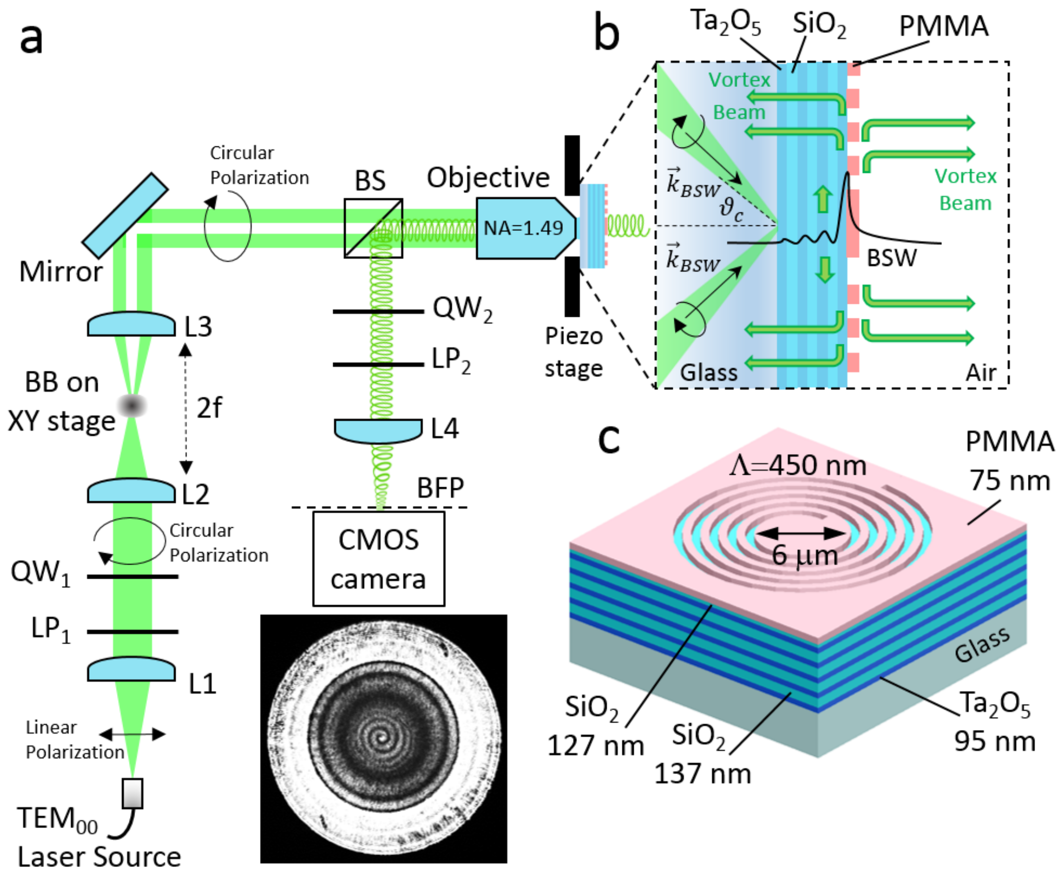

Figure 1. a) Sketch of the experimental setup. $L_{1\text{-}4}$ Plano-Convex lenses, $LP_{1,2}$ Polarizers, $QW_{1,2}$ Quarter-wave Plates, BB Beam Blocker, BS Beamsplitter, BFP Back Focal Plane. In the exemplary BFP image, an interference pattern is shown, due to the superposition of a diffracted vortex beam and a reflected spherical wave from the sample surface. No Beam Blocker has been used in this case. b) Detailed view of the BSW coupling and diffraction mechanism. Illumination is provided by means of a beam-blocked circularly polarized laser beam focused through an oil immersion objective, such that the minimum incidence angle is slightly above the critical angle θ_c, in order to match the BSW coupling conditions. c) Sketch of the multilayer structure with an exemplary spiral diffraction grating fabricated in PMMA on top (not to scale).

RESULTS AND DISCUSSION

In this section, experimental results are presented related to (i) a circular-symmetric annular grating with topological charge m=0, (ii) a single-arm spiral grating, (iii) a double-arm spiral grating. In the last two cases, both handedness of the incident polarization are considered, namely Right-Handed Circular (RHC) and Left-Handed Circular (LHC) polarizations, such that the incident beam Spin Angular Momentum (SAM) and the grating topological charge can have either equal or opposite sign. In order to evaluate the polarization state of the diffracted light, the polarization ellipse parameter $\varepsilon(k_x, k_y) = \frac{1}{2} arg\left(\sqrt{S_1^2 + S_2^2} + iS_3\right)$ is calculated across the BFP, where S_1, S_2 and S_3 are the Stokes parameters [40]. Right-Handed Circular (RHC), Left-Handed Circular (LHC) and Linear Polarizations (LP) correspond to $\varepsilon_{RHC} = \frac{\pi}{4}$, $\varepsilon_{LHC} = -\frac{\pi}{4}$ and $\varepsilon_{LP} = 0$ respectively. Polarization-filtered raw images and Stokes parameter distributions for the structures considered here are shown in the Supporting Information.

A numerical 3D model based on a commercial Finite-Difference Time-Domain (FDTD) solver (Lumerical Inc.) is used to support the interpretation of the experimental observations. In order to mimic the focused circularly polarized beam underlying the BSW coupling, a pair of (coherent) linear orthogonal dipoles laying on the multilayer plane and oscillating with a $\frac{\pi}{2}$ relative phase delay are introduced (see Supporting Information Movie S2). Further details on the validity of this model are provided in the Methods section.

Circular Outcoupler (m=0). In this configuration, a RHC circular polarization ($\varepsilon = \frac{\pi}{4}$) is employed to couple BSWs that are then diffracted. As shown in Figure 2a,e, the total intensity collected on the BFP exhibits a maximum at $k_x = k_y = 0$, corresponding to a constructive interference condition for light traveling along a direction perpendicular to the multilayer surface. A linear-polarization filtering reveals the presence of a pair of spiral-like arms spreading from the central maximum that rotate as the polarization analyser is rotated (in Figure 2b,e the measured and calculated intensity of the x-component of the diffracted light are presented). Without the polarization filter, the spiral-like arms merge together to form a ring surrounding the central maximum. When polarization-projected onto a RHC polarization state, the intensity pattern has still a maximum in the BFP center (Figure 2c,g), while a weak ring is obtained for a projection onto a LHC polarization state (Figure 2d,h). A comparison between the distributions for the measured and the calculated parameter $\varepsilon(k_x, k_y)$ on the BFP indicates that the central maximum is substantially RHC polarized, i.e. $\varepsilon(0,0) \cong \frac{\pi}{4}$, while the outer ring is LHC polarized, i.e. $\varepsilon(0,0) \cong -\frac{\pi}{4}$ (Figure 2i,l).

By enforcing the conservation of the Total Angular Momentum *J*, which also takes into account the topological charge m imparted by the diffraction grating, the following equation applies: $\sigma_i + m = 1 + 0 = \sigma_o + \ell$, where σ_o is the output SAM number and ℓ is the corresponding OAM number. The solution to this equation is not unique. In particular, two SAM-OAM configurations are possible: a RHC beam preserving the input polarization and carrying zero OAM, i.e. $\sigma_o = +1$ and $\ell = 0$, and a doughnut LHC beam with a reverse polarization, with $\sigma_o = -1$ and OAM with $\ell = +2$. The two beams are partially overlapped. This observation is supported by the phase distribution calculated for the RHC and the LHC polarized fields presented in Figure 2m,n: a flat wavefront with constant phase is found for the RHC beam ($\ell = 0$) and a spiral wavefront with two 2π discontinuities for the LHC beam ($\ell = +2$).

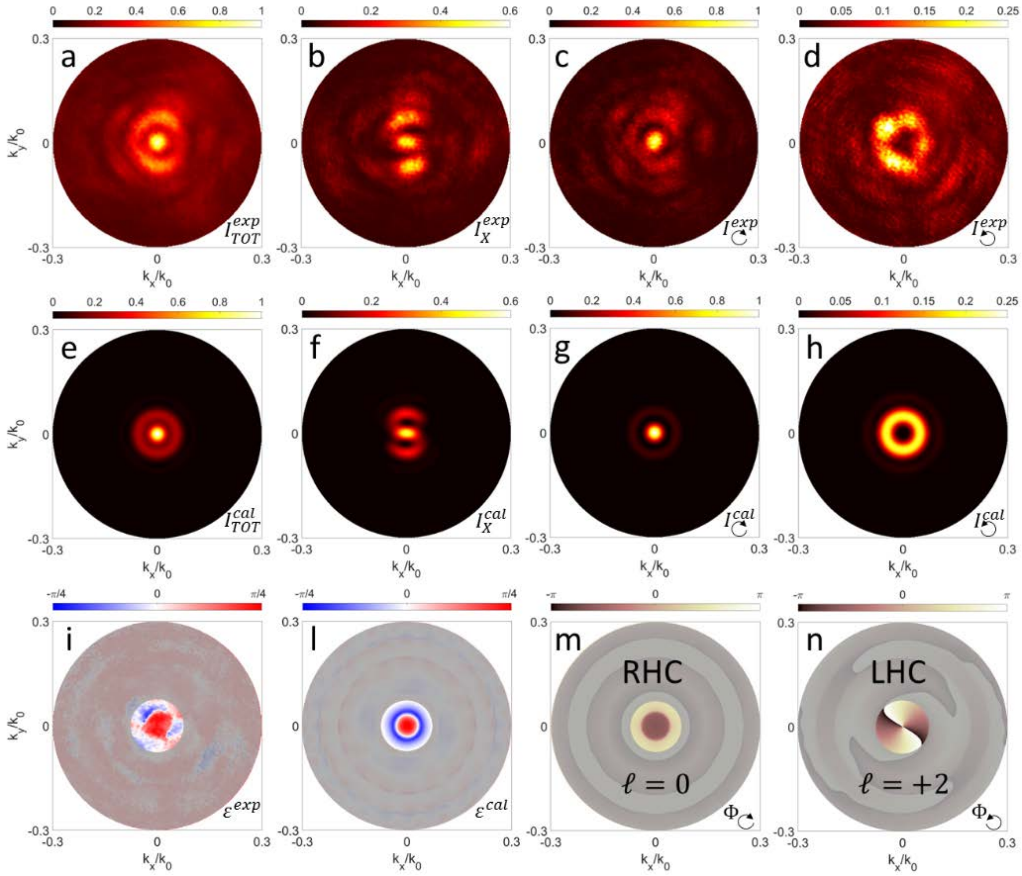

Figure 2. BFP Diffraction patterns from a circular outcoupler ($m = 0$). Incident polarization is RHC. a,e) experimental and calculated total intensity showing a central spot surrounded by a weak outer ring; b,f) experimental and calculated x-polarized intensity; c,g) experimental and calculated RHC intensity showing a central spot; d,h) experimental and calculated LHC intensity showing a doughnut shape; i,l) experimental and calculated polarization ellipse parameter $\varepsilon(k_x, k_y)$ with the sign reversal from the inner area to the outer ring; m) calculated phase of the diffracted field with RHC polarization, showing a constant distribution; n) calculated phase of the diffracted field with LHC polarization, showing two 2π discontinuities.

Spiral Outcoupler ($\boldsymbol{m = -1}$). BSWs are first coupled with an input RHC polarization ($\sigma_i = +1$) and made interacting by a spiral grating with opposite handedness ($m = -1$). The corresponding intensity pattern is shown in Figure 3a,e.

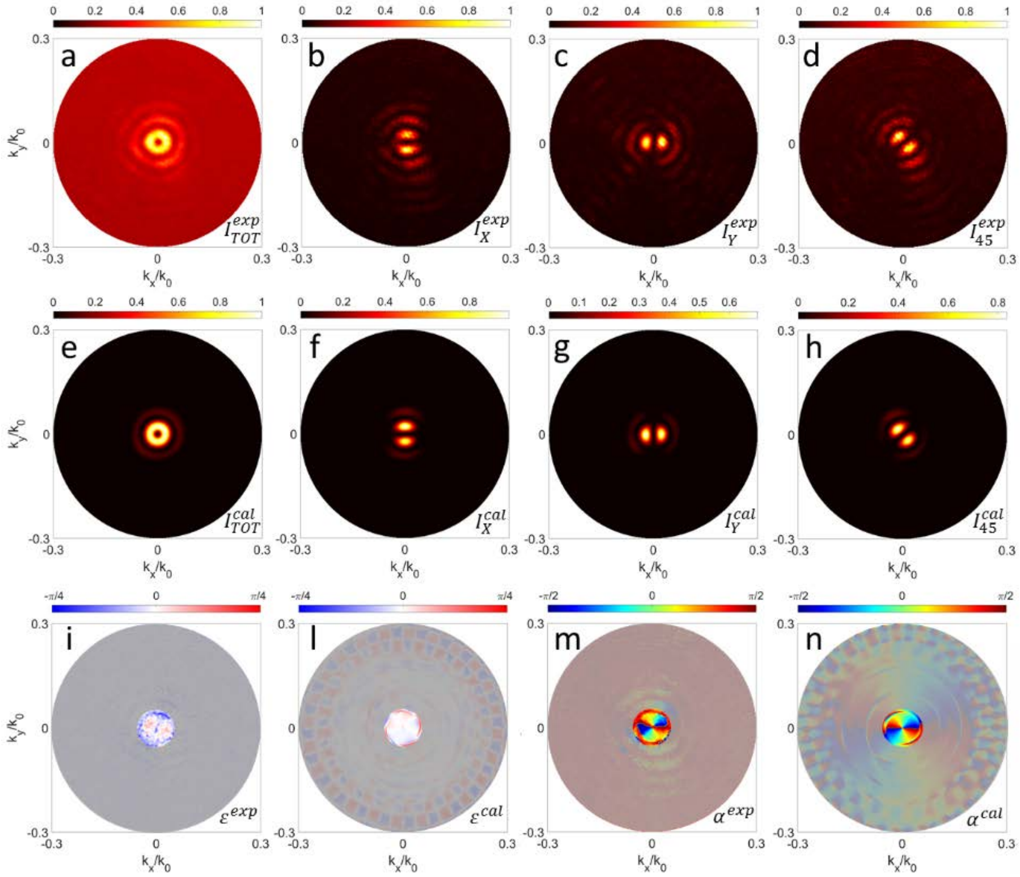

Figure 3. BFP Diffraction patterns from a 1-arm spiral outcoupler ($m = -1$). Incident polarization is RHC. a,e) experimental and calculated total intensity showing a doughnut shape; b,f) experimental and calculated x-polarized intensity; c,g) experimental and calculated y-polarized intensity; d,h) experimental and calculated 45°-polarized intensity; i,l) experimental and calculated polarization ellipse parameter $\varepsilon(k_x, k_y)$ indicating a substantially linear polarization state $\varepsilon \cong 0$; m,n) experimental and calculated ellipse parameter $\alpha(k_x, k_y)$ indicating an azimuthal orientation of the electric field.

The phase delay profile imparted by the diffractive structure onto the diffracted BSWs results in a destructive interference such that a zero-intensity phase singularity is produced at $k_x=k_y=0$. When filtered with the linear polarizer LP_1 (e.g. oriented along the x, y or 45° direction), two-lobe patterns are found, whose orientation is perpendicular to the analyser transmission axis (Figures 3b-d). Calculated intensity patterns are in good agreement with the experimental observations (Figures 3f-h). The distribution of the parameter $\varepsilon(k_x, k_y)$ shows a substantially linear polarization corresponding to the doughnut ($\varepsilon \cong 0$) (Figures 3i,l). The uniformity of the polarization orientation is evaluated by extracting the parameter $\alpha\left(k_x, k_y\right) = \frac{1}{2} arg(S_1 + iS_2)$, which provides the local orientation of the polarization ellipse (almost a line, in this case) across the BFP [40]. In Figures 3m,n both the experimental and the calculated distributions for $\alpha\left(k_x, k_y\right)$ indicate that the substantially linear polarization follows an axis-symmetric distribution such that the electric field is azimuthally oriented about the beam axis in $k_x = k_y = 0$. In this case, the J conservation rule reads as $\sigma_i + m = 1 - 1 = \sigma_o + \ell = 0$, leading to an output SAM number $\sigma_o = 0$ and an OAM $\ell = 0$, which is consistent with the observed azimuthal polarization state of the output beam.

When the illumination polarization is switched to LHC ($\sigma_i = -1$) the input SAM and the grating topological charge possess the same sign. The overall intensity pattern having a doughnut shape is presented in Figure 4a,e. At a closer look, the output results from the superposition of a pair of ring-shaped beams, which are non-interfering because of their orthogonal polarizations. A weak outer ring (Figure 4c,g) is imaged upon RHC filtering, while an intense inner ring (Figure 4d,h) is obtained upon LHC filtering. The experimental and the calculated distributions for $\varepsilon(k_x, k_y)$ (Figure 4i,l) confirm that the polarization state of the two beams is still substantially circular. However, a reversal of handedness from LHC to RHC can be found while moving from the inner ring toward the outer.

The two partially overlapped beams must satisfy the J conservation rule, i.e. $\sigma_i + m = -1 - 1 = \sigma_o + \ell = -2$. A first solution to this equation is represented by a LHC polarized beam having the same SAM number as the incident radiation $\sigma_o = -1$ and OAM $\ell = -1$. An orthogonal solution is a RHC polarized beam having a reversed SAM $\sigma_o = +1$ and OAM $\ell = -3$. The topological charge of the diffracted vortex beams can be directly appreciated from the calculated phase distributions of the RHC and LHC polarized beams (Figure 4m,n), exhibiting three and one 2π discontinuities respectively, on the BFP.

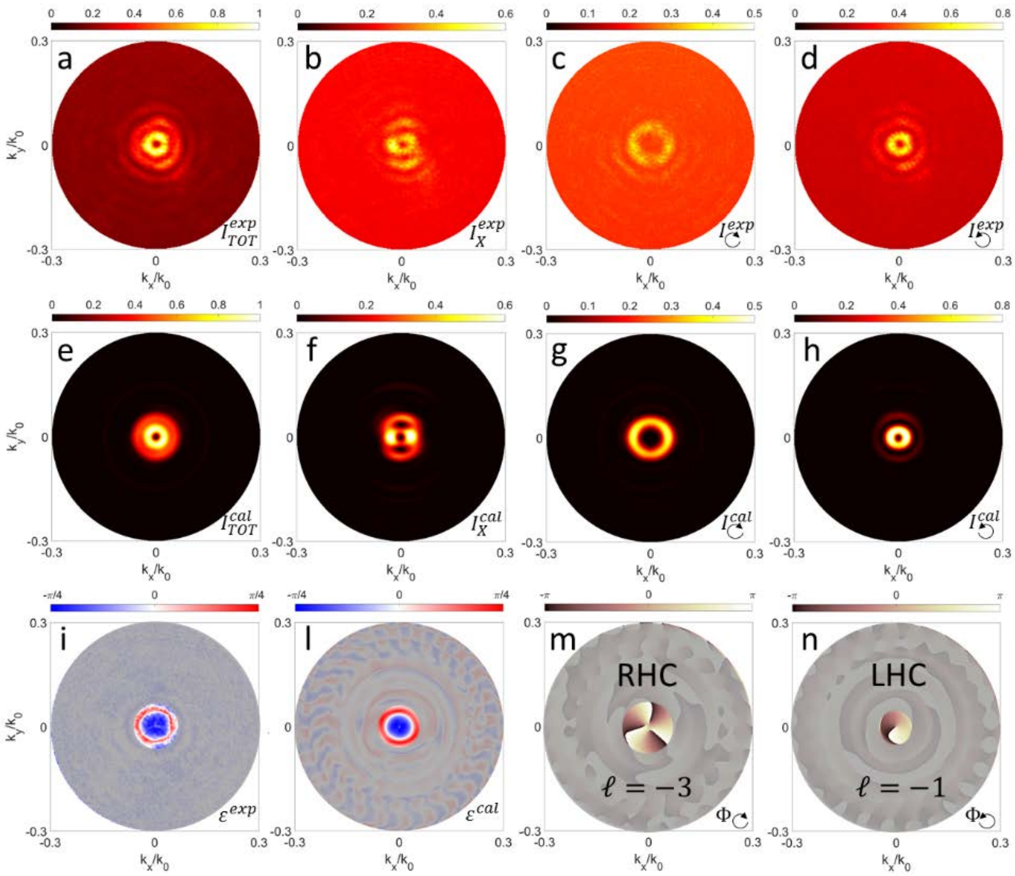

Figure 4. BFP Diffraction patterns from a 1-arm spiral outcoupler ($m = -1$). Incident polarization is LHC. a,e) experimental and calculated total intensity showing a superposition of an inner and an outer ring-shaped patterns; b,f) experimental and calculated x-polarized intensity; c,g) experimental and calculated RHC intensity, distributed according to the outer ring; d,h) experimental and calculated LHC intensity; distributed according to the inner ring; i,l) experimental and calculated polarization ellipse parameter $\varepsilon(k_x, k_y)$ indicating a substantially circular polarization with handedness reversal from the inner to the outer ring; m) calculated phase of the diffracted field with RHC polarization, showing three 2π discontinuities; n) calculated phase of the diffracted field with LHC polarization, showing one 2π discontinuity.

Spiral Outcoupler ($m = -2$). As in the previous configuration, an incident RHC polarization ($\sigma_i = +1$) is first considered. The overall intensity shown in Figure 5a,e is obtained as the superposition of a weak outer ring and a brighter central spot. Both patterns can be individually imaged by operating a polarization filtering through a RHC state (Figure 5c,g) and a LHC state (Figure 5d,h), respectively.

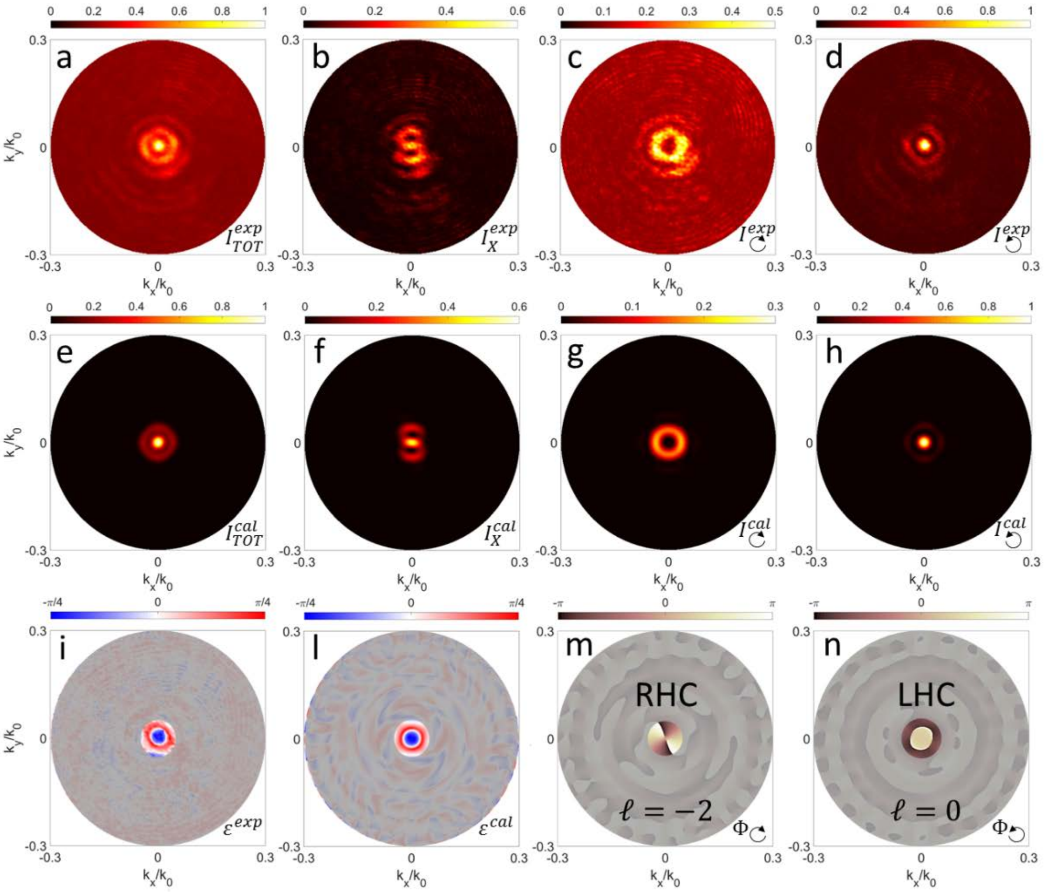

Figure 5. BFP Diffraction patterns from a 2-arms spiral outcoupler ($m = -2$). Incident polarization is RHC. a,e) experimental and calculated total intensity, given by the superposition of a central spot an a weaker outer ring; b,f) experimental and calculated x-polarized intensity; c,g) experimental and calculated RHC intensity, distributed according to the weak outer ring; d,h) experimental and calculated LHC intensity, distributed according to the bright central spot; i,l) experimental and calculated polarization ellipse parameter $\varepsilon(k_x, k_y)$ indicating a substantially circular polarization, with handedness reversal from the central spot to the outer ring; m) calculated phase of the diffracted field with RHC polarization, showing two 2π discontinuities; n) calculated phase of the diffracted field with LHC polarization, showing a uniform phase distribution.

The distribution of the parameter $\varepsilon(k_x, k_y)$ indicates that the polarization is substantially circular across the pattern. However, the bright central spot shows a LHC polarization state, which is reversed with respect to the incident radiation (Figure 5i). Furthermore, the outer weak ring maintains a LHC polarization, as the illumination (Figure 5l). The conservation of the momentum J leads to $\sigma_i + m = +1 - 2 = \sigma_o + \ell = -1$, which has the following two solutions associated to the observed beams:

$\sigma_o = +1$ (RHC) and $\ell = -2$; $\sigma_o = -1$ (LHC) and $\ell = 0$. The calculated phase distributions are consistent with the Total Angular Momentum algebra, since the RHC beam has a vortex wavefront with two 2π discontinuities, while the LHC beam has a flat wavefront (Figure 5m,n). A constant phase is also consistent with the existence of a central maximum at $k_x = k_y = 0$ for the LHC beam. For a LHC polarization ($\sigma_i = -1$) a phase singularity is produced on the optical axis, and the overall intensity pattern (Figure 6a,e) results from the superposition of a LHC polarized inner ring (Figure 6c,g) and a RHC polarized outer ring (Figure 6d,h).

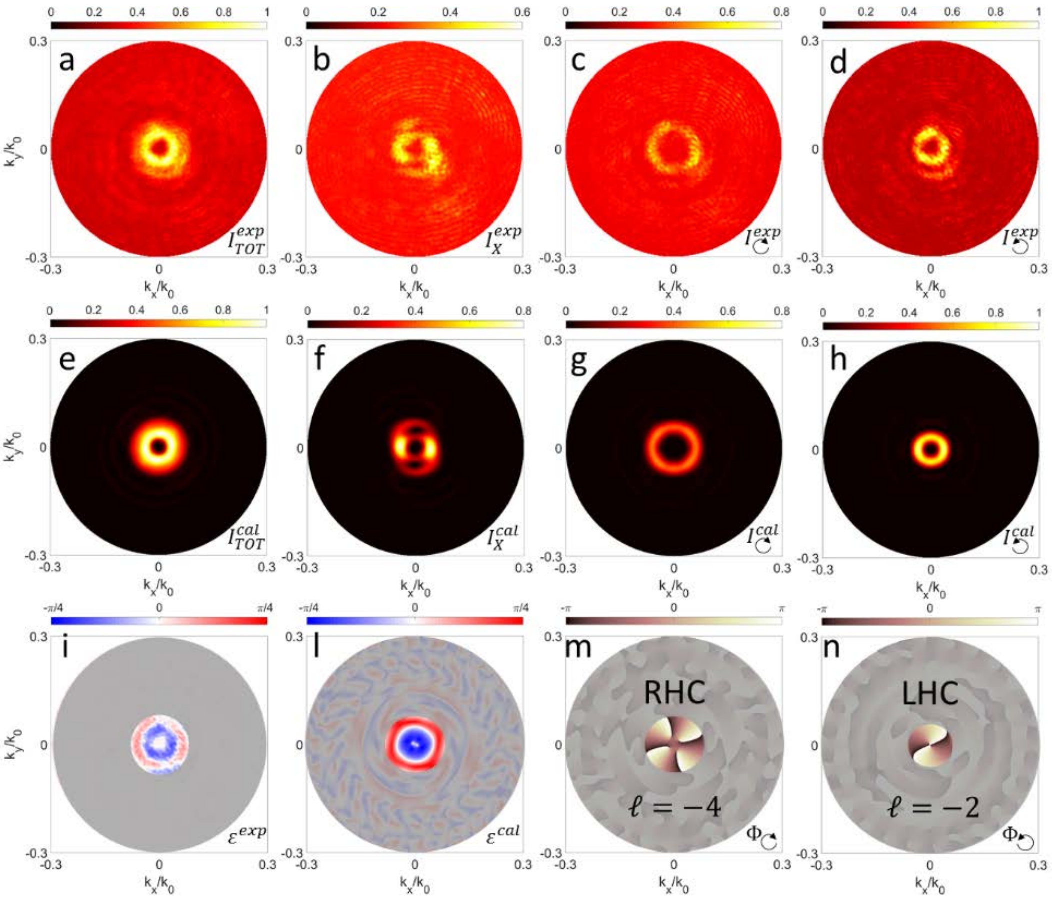

Figure 6. BFP Diffraction patterns from a 2-arm spiral outcoupler ($m = -2$). Incident polarization is LHC. a,e) experimental and calculated total intensity; b,f) experimental and calculated x-polarized intensity; c,g) experimental and calculated RHC intensity; d,h) experimental and calculated LHC intensity; i,l) experimental and calculated polarization ellipse parameter $\varepsilon(k_x, k_y)$; m) calculated phase of the diffracted field with RHC polarization showing four 2π discontinuities; n) calculated phase of the diffracted field with LHC polarization, showing two 2π discontinuities.

Measured and calculated $\varepsilon(k_x, k_y)$ show the handedness reversal occurring when departing from the optical axis toward larger propagation angles, wherein the inner ring preserves the same polarization as the incident radiation (Figure 6i,l). From the conservation of the momentum J, we have: $\sigma_i + m = -1 - 2 = \sigma_o + \ell = -3$, which has the following solutions: $\sigma_o = +1$ (RHC) and $\ell = -4$; $\sigma_o = -1$ (LHC) and $\ell = -2$. In this case, both beams exhibit a phase vorticity, with four 2π discontinuities for the RHC (Figure 6m) state and two 2π discontinuities for the LHC state (Figure 6n).

CONCLUSION

To conclude, a new mechanism for the generation of vectorial vortex beams has been presented, based on spin-orbit interactions involving coupling and diffraction of BSWs. Generally speaking, this kind of effects relies on the coherence characteristics of the radiation involved. For this reason, we employed a laser beam as an external free-space radiation for coupling BSWs that are subsequently diffracted, with an imparted geometrical phase. Several combinations of polarization states and OAM are obtained, as summarized in Table 1. Further options for vortex beam generation carrying OAM with other polarization configurations can be possibly produced by means of multilayers supporting TM-polarized, in addition to TE-polarized BSWs [41].

	Grating Topological Charge m	$\boldsymbol{m = 0}$	$\boldsymbol{m = -1}$	$\boldsymbol{m = -2}$
Incident SAM σ_i				
$\boldsymbol{\sigma_i = +1}$		$\sigma_o = -1$ & $\ell = +2$ $\sigma_o = +1$ & $\ell = 0$	$\sigma_o = 0$ & $\ell = 0$	$\sigma_o = -1$ & $\ell = 0$ $\sigma_o = +1$ & $\ell = -2$
$\boldsymbol{\sigma_i = -1}$		$\sigma_o = -1$ & $\ell = 0$ $\sigma_o = +1$ & $\ell = -2$	$\sigma_o = -1$ & $\ell = -1$ $\sigma_o = +1$ & $\ell = -3$	$\sigma_o = -1$ & $\ell = -2$ $\sigma_o = +1$ & $\ell = -4$

Table 1. Summary of the SAM-OAM combinations obtained by diffraction of BSWs coupled from either RHC or LHC polarized incident light.

The numerical model developed here suggests that the presented approach is likely to work regardless of the coupling mechanism for BSWs. For example, in the perspective of advanced engineered light sources for free-space applications, BSWs can be launched from a single emitter on the multilayer surface by virtue of near-field interactions (so-called BSW-coupled emission) [42,43]. Then, chiral diffractive structures can be used as outcouplers surrounding single sources or even planar BSW cavities (e.g. as described in ref. [44]) hosting light sources within. Provided the coherence requirements for the BSW-coupled radiation leaking out of the cavity are satisfied, the diffraction mechanism for free-space vortex generation remains as reported in the text above. While nanocavities can be chiral themselves, with a handedness-depending LDOS [45], it has been recently shown that chiral plasmonic structures can foster sources located on their surface to radiate according to a specific circular polarization handedness [46]. These strategies provide an unprecedented degree of control on the polarization state of the emitted light. The use of BSWs as a mean for coupling and transferring energy from sources to free-space, mediated by chiral diffractive gratings, can contribute to enhance the performance of purely plasmonic nanostructures, which are often limited by the strong absorption occurring at visible frequencies.

METHODS

Experimental setup. A TEM_{00} doubled-frequency Nd:YAG laser beam (GEM, Laser Quantum) is collimated (L_1) and transmitted through a first polarization-control box, consisting of a linear polarizer LP_1 and a quarter wave plate QW_1. Circular polarization states with both handedness (RH and LH) are generally produced. A beam blocker is introduced in order to spatially filter the laser beam, such that an illumination above the glass/air critical angle θ_c is provided only. The incoming beam is focused onto a flat area on the top surface of the multilayer through a $NA = 1.49$ objective (Nikon Apo TIRF 1003) that is back-contacted to the glass substrate of the sample. The sample holder is mounted on a 3-axis piezo stage. When measuring the diffraction patterns from the spiral gratings, the excitation laser is accurately focused onto the geometric center of the diffraction gratings. Diffracted light on the glass side is collected by the same objective and directed toward the collection arm of the setup, after passing through a 50/50 beam splitter. A second polarization-control box consisting of a quarter wave plate QW_2 and a linear polarizer LP_2 filters the outgoing wave onto the desired polarization state (RHC, LHC or LP). Subsequently, the lens L4 images the BFP of the objective onto a CMOS camera (Thorlabs HR-CMOS DCC3260M). With no Beam Blocker, an interference pattern appears in the BFP image, due to the superposition of the light reflected by the multilayer inside the light cone ($NA \leq 1$) with the diffracted BSW patterns, eventually carrying OAM. As a result, spiral-like interference fringes can be observed depending on the OAM number ℓ, as shown in Figure S3 [32].

Sample fabrication. The 1DPC consists of a dielectric multilayer made of a stack of Ta_2O_5 (high refractive index) and SiO_2 (low refractive index) layers, deposited on a glass coverslip (150 μm thickness) by plasma ion-assisted deposition under high vacuum conditions (APS904 coating system, Leybold Optics). The stack sequence is substrate-[Ta_2O_5-SiO_2]x6-Ta_2O_5-SiO_2-PMMA with 15 layers in total, including PMMA. The Ta_2O_5 layer (refractive index n_{Ta2O5}=2.08) is 95 nm thick, the SiO_2 layer (refractive index n_{SiO2}=1.46) is 137 nm thick. The top SiO_2 layer on top of the stack is 127 nm thick. On top of the structure a 75 nm thick layer of PMMA is spun for pattern fabrication (n_{PMMA}=1.48). Chiral diffractive structures are fabricated by electron beam lithography.

Numerical modeling. Numerical modeling is performed using the Finite-Difference Time-Domain method in the Lumerical Inc. software. In order to mimic the focused circularly polarized light coupling to BSWs, a pair of orthogonal dipolar emitters are positioned at the geometric center of the spiral grating. More specifically, the emitters are placed 10 nm above the PMMA layer, with the dipole momentum laying parallel to the multilayer surface, such that the TE polarization of the BSW can be matched. The two oscillators are phase-shifted by $\pm\pi/2$. In this way, thanks to a near-field interaction, part of the radiated energy from the dipoles is transferred to BSWs (BSW-coupled emission). As shown in Figure S1 and Supporting Movie S2, resulting BSWs are radially propagating, with a spiral wavefront due to the time-varying polarization matching conditions of the field given by the coherent sum of the radiation from the two dipoles.

The diffraction gratings are modeled as circular or spiral grooves in the PMMA layers, with a spatial period Λ=450 nm. The total simulation region has dimensions (15×15×2.6) μm^3. Boundary conditions are set as perfectly matched layers. The smallest mesh size is 23 nm. The electromagnetic near-field is collected using a spatial monitor over a plane 20 nm above the PMMA layer. A near-to far-field projection technique is applied to calculate the field at a distance of 1 m from the structure, on the air side. A cylindrical Perfect Electric Conductor, placed 50 nm above the dipole sources, have been introduced in order to avoid the direct free-space emission from the sources, which could produce interference with the BSW-diffracted radiation we want to investigate. This metallic plate mimic the role of the Beam Blocker in the experimental setup. With this arrangement, only the air-side far-field patterns are calculated. However, as the propagation angles of the diffracted beams (with respect to the multilayer normal) are very small, the refraction effects are negligible and the far-field patterns are expected to be similar to those on the glass substrate side.

ACKNOWLEDGEMENTS

This research has been supported by the project FOCUS from the Règion Bourgogne Franche-Comté and by grants R01 GM125976 and R21 GM129561 from the National Institute of Health. Part of this work has been carried out at Nanofacility INRiM, a laboratory supported by the Compagnia di San Paolo foundation.

REFERENCES

(1) Yao, A.M.; Padgett. M.J. Orbital angular momentum: origins, behavior and applications. *Adv. Opt. Photon.* **2011**, 3, 161-204.

(2) Shen, Y.; Wang, X.; Xie, Z.; Min,C.; Fu, X.; Liu Q.; Gong, M.; Yuan, X. Optical vortices 30 years on: OAM manipulation from topological charge to multiple singularities. *Light: Science & Applications* **2019**, 8, 90.

(3) Yi, X.; Liu, Y.; Ling, X.; Zhou, X.; Ke, Y.; Luo, H.; Wen, S.; Fan, D. Hybrid-order Poincare sphere. *Physical Review A* **2015**, 91, 023801.

(4) Ng, J.; Lin, Z.; Chan, C.T. Theory of Optical Trapping by an Optical Vortex Beam. *Physical Review Letters* **2010**, 104, 103601.

(5) Cojoc, D.; Garbin, V.; Ferrari, E.; Businaro, L.; Romanato, F.; Di Fabrizio, E. Laser trapping and micro-manipulation using optical vortices, *Microelectronic Engineering* **2005**, 78–79,125-131.

(6) Ma, Y.; Rui, G.; Gu, B.; Cui, Y. Trapping and manipulation of nanoparticles using multifocal optical vortex metalens. *Scientific Reports* **2017**, 7, 14611.

(7) Cai, X.; Wang, J.; Strain, M.J.; Johnson-Morris, B.; Zhu, J.; Sorel, M.; O'Brien, J.L.; Thompson, M.G.; Yu, S. Integrated compact optical vortex beam emitters. *Science* **2012**, 6, 338-363.

(8) Xie, Z.; Lei, T.; Li, F.; Qiu, H.; Zhang, Z.; Wang, H.; Min, C.; Du, L.; Li, Z.; Yuan, X. Ultra-broadband on-chip twisted light emitter for optical communications. *Light: Science & Applications* **2018**, 7, 18001

(9) Wei, S.; Lei, T.; Du, L.; Zhang, C.; Chen, H.; Yang, Y.; Zhu, S.W.; Yuan, X.-C. Sub-100nm resolution PSIM by utilizing modified optical vortices with fractional topological charges for precise phase shifting. *Optics Express* **2015**, 23, 30143-30148.

(10) Chen, L. X.; Lei, J.J.; Romero, J. Quantum digital spiral imaging. *Light: Science & Applications* **2014**, 3, e153.

(11) Wang, J.; Yang, J.-Y.; Fazal, I.M.; Ahmed, N.; Yan, Y.; Huang, H.; Ren, Y.; Yue, Y.; Dolinar, S.; Tur, M.; Willner, A.E. Terabit free-space data transmission employing orbital angular momentum multiplexing. *Nature Photonics* **2012**, 6, 488–496.

(12) Ruffato, G.; Massari, M.; Romanato, F. Diffractive optics for combined spatial-and mode-division demultiplexing of optical vortices: design, fabrication and optical characterization. *Scientific reports* **2016**, 6, 24760.

(13) Wang, X.; Nie, Z.; Liang, Y.; Wang, J.; Li, T.; Jia, B. Recent advances on optical vortex generation. *Nanophotonics* **2018**, 7, 1533-1556.

(14) Marrucci, L.; Manzo, C.; Paparo, D. Optical Spin-to-Orbital Angular Momentum Conversion in Inhomogeneous Anisotropic Media. *Physical Review Letters* **2006**, 96, 163905.

(15) Moreno, I.; Davis, J.; Ruiz, I.; Cottrell, D. Decomposition of radially and azimuthally polarized beams using a circular-polarization and vortex-sensing diffraction grating. *Optics Express* **2010**, 18, 7173-7183.

(16) Cardano, F.; Karimi, E.; Slussarenko, S.; Marrucci, L.; de Lisio. C.; Santamato, E. Polarization pattern of vector vortex beams generated by q-plates with different topological charges. *Applied Optics* **2012**, 51, C1-C6.

(17) Genevet, P.; Lin, J.; Kats, M.A.; Capasso, F. Holographic detection of the orbital angular momentum of light with plasmonic photodiodes. *Nature Communications* **2012**, 3, 1278.

(18) Lin, J.; Genevet, P.; Kats, M.A.; Antoniou, N.; Capasso, F. Nanostructured holograms for broadband manipulation of vector beams. *Nano Letters* **2013**, 13, 4269-4274.

(19) Zhan, A.; Colburn, S.; Trivedi, R.; Fryett, T.K.; Dodson, C.M.; Majumdar, A. Low-Contrast Dielectric Metasurface Optics. *ACS Photonics* **2016**, 3, 209-214.

(20) Zhou, Y.; Gao, H.; Teng, J.; Luo, X.; Hong, M. Orbital angular momentum generation via a spiral phase microsphere. *Optics Letters* **2018**, 43, 34-37.

(21) Yue, F.; Wen, D.; Xin, J.; Gerardot, B.D.; Li, J.; Chen, X. Vector Vortex Beam Generation with a Single Plasmonic Metasurface. *ACS Photonics* **2016**, 3, 1558−1563.

(22) Huang, Y.-W.; Rubin, N.A.; Ambrosio, A.; Shi, Z.; Devlin, R.C.; Qiu, C.-W.; Capasso, F. Versatile total angular momentum generation using cascaded J-plates. *Optics Express* **2019**, 27, 7469-7484.

(23) Bouchard, F.; De Leon, I.; Schulz, S.A.; Upham, J.; Karimi, E.; Boyd, R.W. Optical spin-to-orbital angular momentum conversion in ultra-thin metasurfaces with arbitrary topological charges. *Applied Physics Letters* **2014**, 105, 101905.

(24) Maguid, E.; Chriki, R.; Yannai, M.; Kleiner, V.; Hasman, E.; Friesem, A.A.; Davidson, N. Topologically Controlled Intracavity Laser Modes Based on Pancharatnam-Berry Phase. *ACS Photonics* **2018**, 551817-1821

(25) Wang, Z.; Wang, Y.; Adamo, G.; Teng, J.; Sun, H. Induced Optical Chirality and Circularly Polarized Emission from Achiral CdSe/ZnS Quantum Dots via Resonantly Coupling with Plasmonic Chiral Metasurfaces. *Laser & Photonics Reviews* **2019**, 13, 1800276.

(26) Kim, H.; Park, J.; Cho, S.-W.; Lee, S.-Y.; Kang, M.; Lee, B. Synthesis and Dynamic Switching of Surface Plasmon Vortices with Plasmonic Vortex Lens. *Nano Letters* **2010**, 10, 529-536.

(27) Rui, G.; Nelson, R.L.; Zhan, Q. Beaming photons with spin and orbital angular momentum via a dipole-coupled plasmonic spiral antenna," *Optics Express* **2012**, 18819-18826.

(28) Yu, H.; Zhang, H.; Wang, Y.; Han, S.; Yang, H.; Xu, X.; Wang, Z.; Petrov, V.; Wang, J. Optical orbital angular momentum conservation during the transfer process from plasmonic vortex lens to light. *Scientific Reports* **2013**, 3, 3191.

(29) Jiang, Q.; Pham, A.; Berthel, M; Huant, S.; Bellessa, J.; Genet, C.; Drezet, A. Directional and Singular Surface Plasmon Generation in Chiral and Achiral Nanostructures Demonstrated by Leakage Radiation Microscopy. *ACS Photonics* **2016**, 3, 1116-1124.

(30) Gorodetski, Y.; Shitrit, N.; Bretner, I.; Kleiner, V.; Hasman, E. Observation of Optical Spin Symmetry Breaking in Nanoapertures. *Nano Letters* **2009**, 9, 3016-3019.

(31) Zhang, B.; Hu, C.; Tang, B.; Hao, J.; Zhang, X.; Sun, M.; Ding, J. Chiral plasmonic lens with Archimedes-spiral distributed nanoslits. *Journal of Nanophotonics* **2019**, 13, 026008.

(32) Gorodetski, Y.; Drezet, A.; Genet, C.; Ebbesen, T.W. Generating Far-Field Orbital Angular Momenta from Near-Field Optical Chirality. *Physical Review Letters* **2013**, 110, 203906.

(33) Robertson, W.M.; May, M.S. Surface electromagnetic wave excitation on one-dimensional photonic band-gap arrays. *Applied Physics Letters* **1999**, 74, 1800.

(34) Liscidini, M.; Galli, M.; Patrini, M.; Loo, R.W.; Goh, M.C.; Ricciardi, C.; Giorgis, F.; Sipe, J. E. Demonstration of diffraction enhancement via Bloch surface waves in a-SiN:H multilayers. *Applied Physics Letters* **2009**, 94, 043117.

(35) Sinibaldi, A.; Fieramosca, A.; Rizzo, R.; Anopchenko, A.; Danz, N.; Munzert, P.; Magistris, C.; Barolo, C.; Michelotti, F. Combining label-free and fluorescence operation of Bloch surface wave optical sensors. *Optics Letters* **2014**, 39, 2947-2950.

(36) Angelini, A.; Barakat, E.; Munzert, P.; Boarino, L.; De Leo, N.; Enrico, E.; Giorgis, F.; Herzig, H.P.; Pirri, C.F.; Descrovi, E. Focusing and extraction of light mediated by Bloch surface waves. *Scientific Reports* **2014**, 4, 5428.

(37) Angelini, A.; Enrico, E.; de Leo, N.; Munzert, P.; Boarino, L.; Michelotti, F.; Giorgis, F.; Descrovi, E. Fluorescence diffraction assisted by Bloch surface waves on a one-dimensional photonic crystal. *New Journal of Physics* **2013**, 15, 073002

(38) Rui, G.; Abeysinghe, D.C.; Nelson, R.L.; Zhan, Q. Demonstration of beam steering via dipole-coupled plasmonic spiral antenna. *Scientific Reports* **2013**, 3, 2237.

(39) Angelini, A.; Munzert, P.; Enrico, E.; De Leo, N.; Scaltrito, L.; Boarino, L.; Giorgis, F.; Descrovi, E. Surface-Wave-Assisted Beaming of Light Radiation from Localized Sources. *ACS Photonics* **2014**, 1, 612–617.

(40) Röhrich, R.; Hoekmeijer, C.; Osorio, C.I.; Koenderink, A.F. Quantifying single plasmonic nanostructure far-fields with interferometric and polarimetric k-space microscopy. *Light-Science & Applications* **2018**, 7, 65.

(41) Pellegrini, G.; Finazzi, M.; Celebrano, M.; Duò, L.; Biagioni, P. Chiral surface waves for enhanced circular dichroism. *Physical Review B* **2017**, 95, 241402.

(42) Liscidini, M.; Galli, M.; Shi, M.; Dacarro, G.; Patrini, M.; Bajoni, D.; Sipe, J.E. Strong modification of light emission from a dye monolayer via Bloch surface waves. *Optics Letters* **2009**, 34, 2318-2320.

(43) Badugu, R.; Mao, A.; Blair, S.; Zhang, D.; Descrovi, E.; Angelini, A.; Huo, Y.; Lakowicz, J.R. Bloch Surface Wave-Coupled Emission at Ultra-Violet Wavelengths. *Journal of Physical Chemistry C* **2016**, 120, 28727-28734.

(44) Stella, U.; Boarino, L.; de Leo, N.; Munzert, P.; Descrovi, E. Enhanced directional light emission assisted by resonant Bloch Surface Waves in circular cavities. *ACS Photonics* **2019**, 6, 2073-2082.
(45) Pham, A.; Berthel, M.; Jiang, Q.; Bellessa, J.; Huant, S.; Genet, C.; Drezet, A. Chiral optical local density of states in a spiral plasmonic cavity. *Physical Review A* **2016**, 94, 053850.
(46) Pachidis, P.; Cote, B.M.; Ferry, V.E. Tuning the polarization and directionality of photoluminescence of achiral quantum dot films with chiral nanorod dimer arrays: implications for luminescent applications. *ACS Applied Nano Materials* **2019**, 2, 5681-5687.

GRAPHICAL TOC ENTRY